fluids

MDPI

Article

RIM-PIV Measurements of Turbulent Flow over a Rough Porous Bed

Zeeshan Qadir Memon * and James Liburdy †

School of Mechanical, Industrial, and Manufacturing Engineering, Oregon State University, Corvallis, OR 97331, USA

* Correspondence: memonz@oregonstate.edu or memon.zeeshan@uolrk.edu.pk

† Deceased Author.

Abstract

Flow over permeable beds is important in sediment transport and mixing processes, yet detailed velocity and stress measurements remain difficult to obtain, particularly close to the sediment–water interface (SWI). In this work, we use refractive-index-matched PIV to study turbulent open-channel flow over and within a permeable bed composed of monodisperse borosilicate glass beads. Measurements are reported for three low-Re_K cases, $Re_K = 0.224$, $Re_K = 0.335$, and $Re_K = 0.360$, to resolve the mean velocity structure and the associated viscous, turbulent, Reynolds, and dispersive stress distributions. The results show that both the mean velocity and the turbulence intensity decrease rapidly below the SWI, indicating strong damping within the porous bed. Above the bed, the flow retains a boundary-layer structure, and increasing Re_K enhances the turbulence intensity without changing the overall regime. The results indicate a shift from turbulent transport above the bed to viscous control within the porous layer, while dispersive stresses peak near the interface. Overall, the SWI controls momentum exchange within a thin region and the porous bed suppresses turbulence penetration into the subsurface.

Keywords: turbulent flow; permeable bed; refractive-index-matched PIV; SWI; double-averaging

1. Introduction

Flow over permeable and porous surfaces is important in many environmental and engineering systems, including riverbeds, hyporheic zones, filtration units, packed beds, and heat transfer devices [1,2]. In all of these systems, the boundary is not impermeable. Fluid can penetrate into the pore space, and that penetration changes the near-interface velocity structure, the balance between viscous and turbulent stresses, and the way momentum is exchanged between the free flow and the porous matrix [3–5]. For this reason, flow over permeable beds cannot be treated simply as a rough-wall problem. The presence of permeability introduces another physical scale, linked to the pore geometry and bed permeability, that modifies the structure of the near-bed flow [6].

In permeable-bed flows, the SWI forms a transition region between the overlying flow and the pore space, and it is within this region that momentum exchange is most significant [7]. Related studies of shallow flow over rough surfaces have also shown that bed geometry can strongly modify velocity structure and momentum exchange near the boundary [8].

Academic Editor: Akira Nakayama

Received: 19 April 2026
Revised: 17 May 2026
Accepted: 22 May 2026
Published: 27 May 2026

Early work on turbulent flow over permeable walls showed that permeability alters both the mean flow and the turbulence field [9]. Breugem et al. [3] used direct numerical simulations to study turbulent channel flow over a permeable wall. The results showed that permeability changes the flow behavior and that the effect is not limited to the viscous region near the wall. But it influences the entire flow domain. They also found changes in the mean velocity profile and modifications in Reynolds stresses. These results are important because a permeable boundary behaves differently from a smooth wall and cannot be simply treated as a shifted origin. Instead, the permeability changes the turbulence structure itself.

Later work placed these observations into a broader physical framework. Ghisalberti and Nepf [10] showed that many flows over obstructed surfaces develop an inflectional mean profile and that such profiles are susceptible to shear-layer instability and the formation of large coherent motions [10]. In permeable-bed flows, the SWI is the location where shear, permeability, and roughness interact. Manes et al. used this framework to examine turbulent boundary layers over permeable walls and showed that permeability changes the scaling and near-wall structure of the flow [4].

Manes et al. [4] and Voermans et al. [5,11] addressed this issue by proposing a classification based on the permeability Reynolds number, $Re_K = u_\tau \sqrt{K}/\nu$. This parameter compares the permeability length scale with the viscous scale and provides a useful way to organize the behavior of flows over permeable beds. Their results showed that at low Re_K, the flow is more strongly damped by viscosity and turbulence penetration into the bed is limited, whereas at larger Re_K, the exchange across the interface becomes more energetic. This classification is important for the present experiments because all cases remain in the low-Re_K range. The expected response is therefore a viscously damped flow with a strong interfacial adjustment region, rather than a transition to deep turbulence penetration [12].

Experimental and numerical studies of hydraulically complex flows, including turbulent flow around artificial reef arrays, have shown that the arrangement of roughness elements can substantially alter turbulence production and near-bed flow structure [13]. Experimental measurements at the SWI have also clarified how turbulence and stress are distributed across the bed boundary. Blois et al. [6] measured flow and turbulence across the SWI and showed that the largest changes occur in a relatively narrow region around the interface. Their measurements showed that the porous bed damps the flow, whereas the shear layer above the bed remains energetic. The findings are consistent with prior studies of permeable beds, which demonstrate that porous beds reduce motion inside the pore spaces, while the overlying free flow maintains a developed turbulent structure. These observations indicate that momentum exchange is concentrated near the interface rather than being uniformly distributed inside the porous layer. The same coupling between near-bed flow, particle-scale resistance, and bed structure is also central to sediment transport problems [14].

Further, Nikora et al. [15] developed the concept of double averaging to interpret flow over rough and permeable beds. Nikora et al. [15] showed that Reynolds averaging alone is not sufficient when the geometry itself creates strong spatial heterogeneity in the time-averaged flow. In such cases, the double-averaging framework is needed to separate the spatially averaged mean flow, turbulent stresses, and form-induced or dispersive stresses. This becomes relevant in flows over rough porous beds where the pore geometry creates spatial heterogeneity in the mean flow and makes the dispersive stresses significant at the interface. For this reason, analyses of permeable-bed flow include not only the mean velocity and Reynolds stresses but also viscous and dispersive stress components [16,17].

Direct numerical simulations near the SWI show that turbulence and hyporheic exchange are strongly controlled by the near-bed geometry and the penetration of stresses into

the porous layer [18]. Pore-resolved simulations of randomly packed, permeable sediment beds show that mean flow penetration, Reynolds stresses, and form-induced stresses vary systematically with Re_K and remain concentrated near the SWI [17]. Continuum modeling of randomly packed beds also provides a basis for testing stress partitioning and velocity decay in rough permeable beds [19].

Despite these advances, detailed experimental measurements remain limited for flow over rough porous beds, and fewer data are available for the flow inside the bed. This limitation is mainly caused by the difficulty of obtaining optical access inside a packed bed while resolving both the overlying flow and the pore space response. Refractive-index-matched particle image velocimetry reduces optical distortion and makes it possible to measure velocity close to and within the pore space. However, there are still relatively few datasets that resolve, in the same controlled experiment, the mean velocity, turbulence intensity, root-mean-square velocity fluctuations, viscous stress, Reynolds stress, and dispersive stress across the SWI [20].

The objective of the present study is therefore to quantify how a rough, monodisperse, permeable bead bed modifies momentum transport across the SWI at low-permeability Reynolds numbers. To address this objective, we use refractive-index-matched PIV in an open-channel flume and apply the double-averaging framework to separate the spatially averaged mean flow, turbulent fluctuations, and form-induced spatial variations. The specific goals are to measure the vertical decay of mean velocity inside the bed, evaluate the relative contributions of viscous, Reynolds, and dispersive stresses, and determine how these quantities change for Re_K values of 0.224, 0.335, and 0.360.

2. Materials and Methods

2.1. Experimental Setup

The experiments were performed in a custom-made recirculating flume at the Experimental Fluid Mechanics Laboratory at Oregon State University. The present study uses a mixture of low-viscosity mineral oil (ASI Standards, Oak Ridge North, TX, USA) and anise oil (commercially supplied as aniseed oil; Aarnav Global Exports, Ghaziabad, Uttar Pradesh, India) as the recirculating fluid. The flume is composed of chemically welded polycarbonate material and measures 1.78 m in length, 0.178 m in width, and 0.18 m in depth. The channel dimensions were selected so that the porous section occupied most of the working length while maintaining optical access from the side of the flume. The channel width is approximately 12 bead diameters, and the bed depth is approximately 10 bead diameters; therefore, the bead pack behaves as a finite porous layer rather than only a single roughness element attached to the wall. The measurement region was located within the bead-bed test section and aligned relative to the SWI, with the field of view extending from the overlying flow into the upper pore layers. The facility arrangement, including the flume, bead bed, pump loop, and optical access, is shown in Figure 1.

The porous bed was constructed from spherical, monodisperse borosilicate glass beads with a nominal diameter of 15 mm, which is a laboratory-scale roughness size appropriate for studying flow over a rough permeable bed in an open-channel configuration. The bed depth was approximately 150 mm, corresponding to about 10 bead layers, and the bed length was $L_B = 1.30$ m. This bed depth reduces the influence of finite bed thickness and provides a developed porous region beneath the SWI. The packing produced a rough porous bed rather than an idealized smooth permeable wall, and the measured porosity remained in the range expected for random packing of spheres. Because the present study focuses on an open-channel flow over a rough bead bed, no bottom imaging window or wall-mitigation arrangement was used beneath the packed bed. We aim to capture the flow above and within the porous layer created by the monodisperse beads.

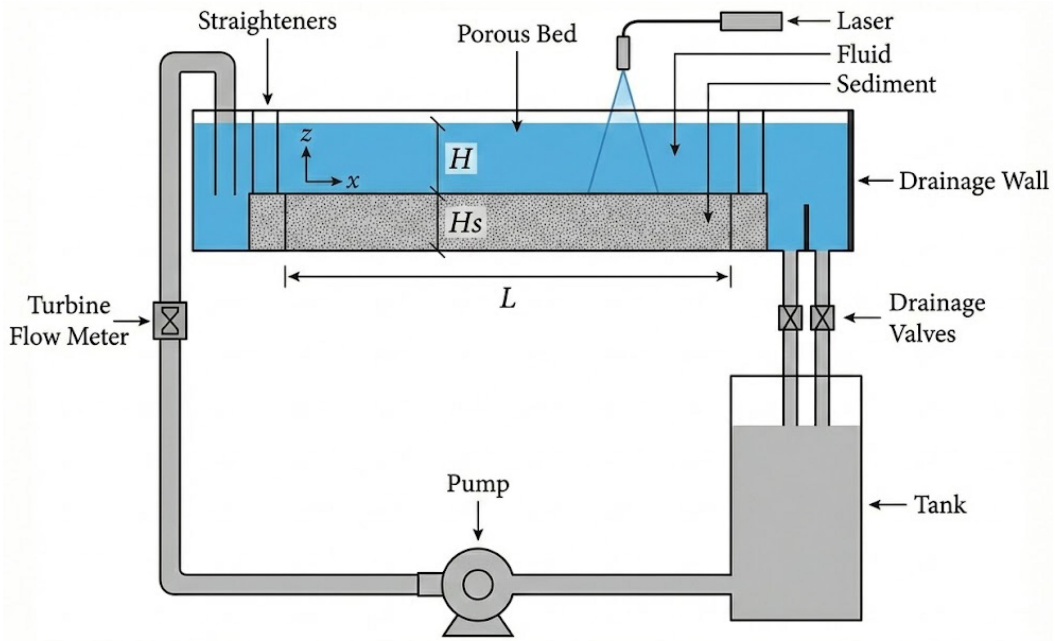

Figure 1. Schematic diagram of the experimental facility, including the recirculating flume, porous bead bed, flow loop, and optical measurement region.

The flume parameters are summarized in Table 1, while the flow conditions are listed separately in Table 2. The ratio L_B/d_p indicates sufficient streamwise length for the bed to behave as a porous layer, and the measurement window covered approximately six bead diameters in the streamwise direction and five bead diameters in the vertical direction. This field of view allowed the spatially averaged profiles to include both the interfacial region and the upper part of the pore space.

Table 1. Geometric and measurement parameters for the RIM-PIV experiments.

Quantity	Value	Relevant Scale
Flume length	1.78 m	Overall recirculating test channel length
Flume width	0.178 m	$W/d_p \approx 12$
Flume depth	0.18 m	Available channel depth
Porous-bed length, L_B	1.30 m	$L_B/d_p \approx 86.7$
Grain diameter, d_p	15 mm	Monodisperse borosilicate glass beads
Measurement window size	$\approx 6d_p \times 5d_p$	Streamwise by vertical field of view
Vector spacing	16 pixels	Approximately 26 vectors per bead diameter
Image pairs per run	6000	Time averaging for each case

Table 2. Experimental flow conditions for the RIM-PIV measurements.

Method	Case	Re_K	u_τ (m s^{-1})	U_∞ (m s^{-1})	Re_H	Re_τ	H_F (m)	H_B (m)
RIM-PIV	1	0.224	0.0025	0.0242	503.723	51.7047	0.100	0.095
RIM-PIV	2	0.335	0.0037	0.0331	690.05	77.226	0.100	0.095
RIM-PIV	3	0.360	0.0040	0.0344	716.763	82.8032	0.100	0.095

Note: H_F is the free-flow depth above the porous bed and H_B is the porous bed height. The Reynolds numbers are defined as $Re_H = U_\infty H_F/\nu$, $Re_\tau = u_\tau H_F/\nu$, and $Re_K = u_\tau\sqrt{K}/\nu$.

Flow was generated by a centrifugal pump (Peerless C-810A pump; Peerless Pump, Indianapolis, IN, USA), connected to an upstream reservoir and controlled using a variable-frequency drive. The flume inlet was flow-conditioned by means of a number of 3D-printed,

perforated grid flow straighteners to reduce secondary currents and obtain a uniform flow velocity distribution. The recirculating system enabled steady flow operation for long durations, which was necessary for the particle image velocimetry measurements reported here.

The flow rate to the flume was continuously monitored using an Omega turbine flow meter (Omega Engineering, Inc., Norwalk, CT, USA; SN:10222795) installed inline with the main flow loop upstream of the test section. The turbine rotation was converted to an electrical signal corresponding to the volumetric flow rate. The transducer and signal-conditioning unit were powered using a Tektronix PS281 DC power supply (Tektronix, Inc., Beaverton, OR, USA), and the conditioned signals were recorded using a National Instruments data acquisition system (NI-DAQ; National Instruments, Austin, TX, USA). A custom LabVIEW-based data acquisition system was used to continuously monitor and record the flow rate in real time during each experiment. Although the use of the mineral oil–anise oil mixture increases viscosity and limits the attainable Reynolds number compared with water, the overlying flow still exhibited measurable turbulent fluctuations, Reynolds stresses, and a persistent shear layer above the SWI. Accordingly, the present cases correspond to turbulent open-channel flow above a viscously damped, low-Re_K porous bed, rather than fully turbulent pore-scale flow throughout the bed.

The RIM-PIV cases performed are reported in Table 2. A right-handed Cartesian coordinate system was used, with the x-axis aligned with the bulk flow direction, the z-axis normal to the bed (positive upward), and the y-axis spanwise across the channel width. The SWI was defined as $z = 0$, with $z > 0$ corresponding to the water column and $z < 0$ to depths within the porous bed.

The shear velocity, or friction velocity, was estimated from the maximum total shear stress, $u_\tau = \sqrt{\frac{\tau_{max}}{\rho}}$, where the total shear stress includes the viscous, Reynolds, and dispersive contributions obtained from the double-averaged velocity field. The permeability, K, of the glass bead pack was estimated using the Kozeny–Carman relation for a randomly packed bed of nearly monodisperse spheres:

$$K = \frac{\epsilon^3 d_p^2}{180(1-\epsilon)^2} \quad (1)$$

where ϵ is the bed porosity and d_p is the bead diameter. The resulting permeability is on the order of 10^{-7} m^2, consistent with the values reported by Strahl [12].

As Re_K remains below unity in all three cases, the flow is expected to remain close to Darcy-dominated resistance within much of the pore space. However, the largest case, $Re_K = 0.360$, approaches the range where weak inertial corrections and departure from purely Darcy behavior may begin locally near the SWI. For this reason, the results are discussed as low-Re_K interfacial-transition cases in which pore scale motion is strongly damped while the overlying flow maintains turbulent transport.

Bead Packing

A porous bed was formed by placing 15 mm monodisperse borosilicate glass beads into the test section. The bed thickness was maintained at 10 bead layers or more to reduce possible wall-blocking effects [21,22]. The resulting bed depth was approximately 150 mm. The beads were packed without imposing a regular lattice, producing a repeatable rough porous bed. For optical access, the RIM optical beads were placed in the upper four layers of the bed within the imaging window, while the bulk of the bed consisted of non-optical glass beads. The flow developed naturally over and within the rough packing formed by the monodisperse beads. This arrangement preserves the hydraulic response of a rough porous layer. The measurements therefore represent flow over and within a porous bead

layer. The beads were kept clean during the experiments. After each run, the oil mixture was filtered several times through our in-house-made filtration system and cleaned the beads using an ultrasonic cleaner to remove wax and accumulated PIV particles. This procedure maintained consistent optical performance during the experiments.

2.2. Velocity Measurements

The camera was oriented with the longer image axis aligned in the streamwise direction and the shorter image axis normal to the bed surface. Measurements achieved a spatial resolution of 36.2 µm/pixel, providing a density of 26 vectors across a single bead diameter. The resulting images covered nearly six bead diameters in the streamwise direction and five bead diameters in the vertical direction. These dimensions are sufficient for applying the double-averaging methodology and minimizing sensitivity to the exact imaging position related to individual beads. The measurement window extended at least two bead diameters below the interface. During the experiments, ambient lighting was turned off to reduce reflections from the beads.

PIV and optical-flow-based processing methods are widely used to resolve turbulent velocity fields with spatial consistency [23]. For each run, 6000 image pairs were acquired at a steady rate of 15 Hz. The raw images were processed in LaVision DaVis 8.4 using a multi-pass cross-correlation algorithm with decreasing interrogation window sizes of 64×64 pixels followed by 32×32 pixels in the final passes. A 50% overlap was applied for all passes, resulting in a final vector spacing of 16 pixels. The pulse separation was adjusted for each experiment. The pulse timing was selected so that the particle displacement remained at approximately one-third of the interrogation window. Based on this criterion, the pulse separation time Δt was kept between 600 and 700 µs. The vector fields generated from raw PIV image pairs were exported to MATLAB R2024a for further computation and plotting. For each case, the instantaneous velocity fields were first time-averaged at each measurement location. The resulting mean and fluctuating velocity fields were then spatially averaged in the streamwise direction to obtain the vertical profiles reported in the Results section. This procedure is consistent with the double-averaging framework and reduces sensitivity to the local arrangement of individual beads within the measurement plane. The SWI used for profile alignment was kept at $z = 0$, with negative z values corresponding to the pore region and positive z values corresponding to the overlying flow.

2.3. Refractive Index Matching

A refractive index matching (RIM) technique was employed to enable particle image velocimetry (PIV) measurements within the porous bed. By matching the refractive indices of the working fluid and solid particles, optical distortions and scattering are minimized. This allows the unobstructed visualization of the interstitial flow and overcomes the opacity of the bed matrix, which would otherwise prevent optical access to the measurement region. Some studies [5,21] have employed high-salinity aqueous solutions, such as sodium iodide (NaI) and sodium thiocyanate (NaSCN), for refractive index matching. However, these fluids are typically hygroscopic and highly corrosive, which can lead to equipment degradation and limit their suitability for long-term experimental use.

Alternatively, the use of light-viscosity mineral oil, with its refractive index adjusted by adding anise seed essential oil, offers a way to alleviate many practical challenges posed by saline options. A mixture of anise oil and mineral oil, each having different refractive indices, was prepared based on the study of Song et al. [24]. The base fluid, anise oil ($\eta = 1.55$), has a higher refractive index, while light mineral oil ($\eta = 1.4567$) was used as a solvent to adjust the refractive index of the mixture. The resulting mixture refractive index, i.e., $\eta = 1.471$, closely matches that of borosilicate glass beads, $\eta = 1.472$.

Following the general approach used in refractive index matching studies, a series of trial mixtures was prepared rather than selecting a single composition at the outset. In practice, small batches of mineral oil–anise oil mixtures were prepared at different proportions and visually compared against the borosilicate glass beads until the clearest optical match was achieved. This procedure is summarized in Figure 2. Figure 2a shows the set of trial mixtures prepared during the screening stage. The purpose of these samples was to identify the composition that minimized visible distortion prior to preparing the full working volume.

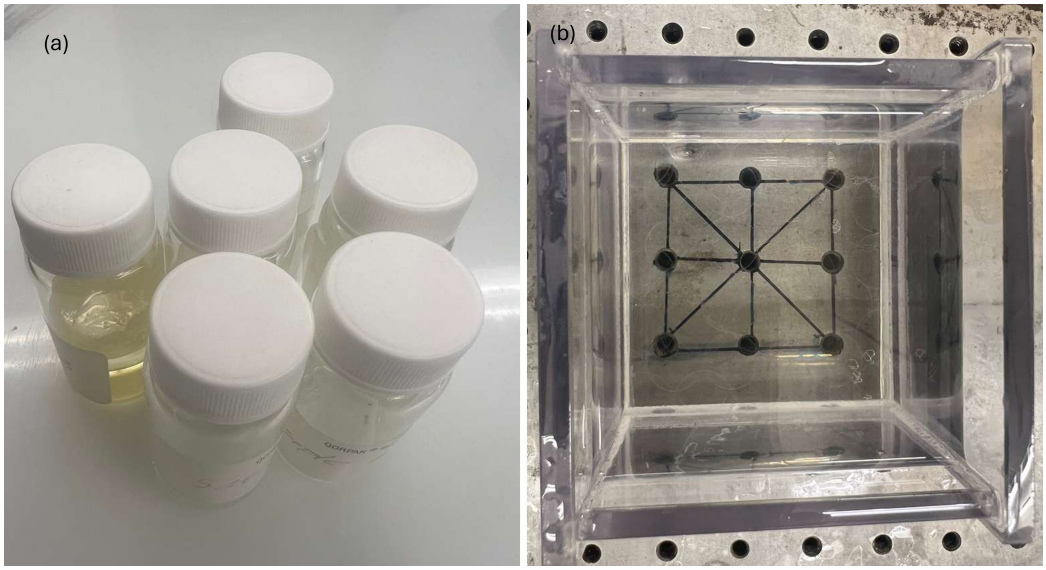

Figure 2. Visual assessment of optical clarity during refractive-index matching: (**a**) trial mixtures prepared at different proportions; (**b**) optical match with glass beads.

Song et al. [24] proposed a correlation for estimating the refractive index of the mixture:

$$\mathrm{RI}_{\mathrm{mixture}} = x \cdot \mathrm{RI}_{\mathrm{anise}} + (1 - x) \cdot \mathrm{RI}_{\mathrm{mineral\ oil}}, \quad (2)$$

where $\mathrm{RI}_{\mathrm{mixture}}$ is the refractive index of the mixture and x is the volume fraction of anise oil. The mixture composition consisted of 20.80% anise oil and 79.20% mineral oil, measured based on mass fraction. The dynamic viscosity of the mixture was experimentally measured at the Oregon State University laboratory and found to be 4.87 mPa s. The density of the fluid mixture was estimated as 885 kg m^{-3}. The refractive index calibration and the corresponding viscosity variation with mixture composition are summarized in Figure 3, which confirms that the selected mixture provides the required optical match while also documenting the associated increase in viscosity.

In refractive-index-matching studies, the working fluid is selected based on both optical and practical considerations. In addition to refractive-index matching, the fluid should provide good optical clarity, minimal image distortion, compatibility with the test materials, and a viscosity suitable for stable experimental operation. The mineral oil–anise oil mixture used here satisfies the optical requirement for borosilicate glass beads and avoids many of the practical problems associated with highly saline or chemically aggressive fluids. However, the mixture also has limitations. The mineral oil–anise oil mixture is more viscous than water, with a viscosity approximately five times larger. The higher viscosity increases flow resistance, requires more pumping power, and results in a limited operating range of Reynolds numbers.

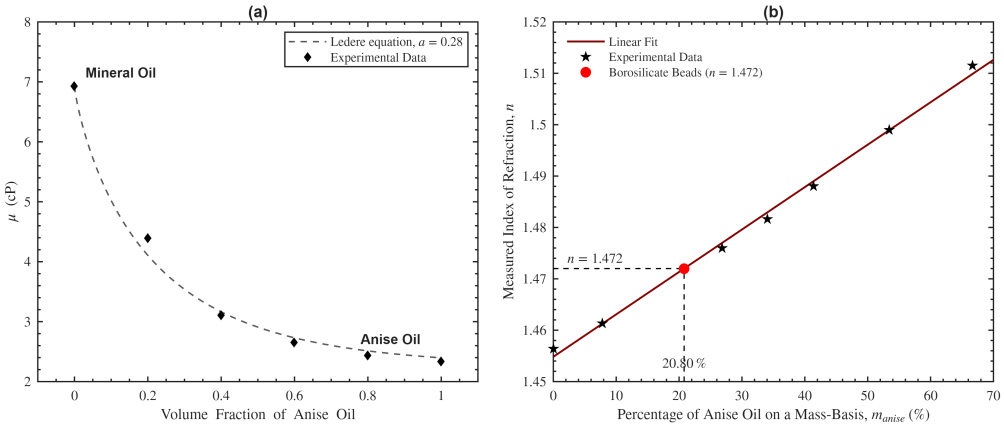

Figure 3. (**a**) Dynamic viscosity of mineral oil–anise oil mixtures as a function of anise oil volume fraction [24]. (**b**) Measured refractive index of the mixture as a function of anise oil mass fraction.

This limitation is common in refractive-index-matching studies because improved optical access can reduce the attainable Reynolds number range. The optical quality of the final mixture is illustrated in Figure 2b. In this image, the container is filled with the mineral oil–anise oil mixture and packed with the glass beads used in the experiments. The bottom support plate, the table surface beneath the cell, and the black guidelines drawn below the test cell remain visible through the bead pack. The image shows that the optical mismatch between the beads and the working fluid is small enough to provide useful visual access through the porous layer. The match is not perfect because the beads remain faintly visible, but the optical clarity is sufficient for PIV measurements near and within the bed. The reduction in attainable Reynolds number is therefore an experimental tradeoff of the RIM approach. In the present study, evidence for the targeted turbulent regime is taken from the measured velocity fluctuations, turbulence-intensity fields, and Reynolds stress profiles above the SWI, while the low Re_K values indicate that turbulence penetration into the porous bed remains strongly limited.

2.4. Double Averaging Methodology

Turbulent flow is inherently three-dimensional and contains a wide range of length scales, from small-scale motions to very-large-scale motions. In flows over rough and permeable beds, conventional Reynolds-averaged descriptions do not always provide an adequate description of the near-bed region. Nikora et al. [15] noted that two-dimensional approximations based only on Reynolds averaging, together with similarity arguments for time-averaged variables, are not generally sufficient in the near-bed region of rough-bed flows. The double-averaging approach addresses this problem by applying averaging in both time and space and retaining additional terms associated with bed geometry and spatial heterogeneity.

A key part of the double-averaging framework is the definition of the spatially averaged instantaneous variable. Following Nikora et al. [15], the intrinsic spatial average may be written as

$$\langle \theta \rangle (x, y, z, t) = \frac{1}{V_f} \int_{V_f} \theta \, dV, \tag{3}$$

and the superficial spatial average may be written as

$$\langle \theta \rangle_s (x, y, z, t) = \frac{1}{V_o} \int_{V_f} \theta \, dV. \tag{4}$$

In Equation (3), θ denotes an instantaneous flow variable, $\langle \cdot \rangle$ denotes spatial averaging, and V_f is the fluid volume within the averaging region. In Equation (4), V_o is the total

averaging volume, including both fluid and solid portions. The intrinsic average therefore represents an average over only the fluid volume, whereas the superficial average represents the fluid contribution normalized by the total averaging volume. These two averages are related by $\langle\theta\rangle_s = \phi\langle\theta\rangle$, where $\phi = V_f/V_o$ is the porosity. Although these relations can also be written using area averaging for planar PIV data, the volume-averaged notation is retained because it is the standard double-averaging form and applies to both the channel region and the interstitial flow within the bed. In the present study, the intrinsic spatial average is used for the reported velocity and stress profiles.

Using Reynolds decomposition, the instantaneous variable is expressed as the sum of a time-averaged part and a fluctuating part,

$$\theta = \overline{\theta} + \theta', \tag{5}$$

and the time-averaged variable can then be decomposed into a spatial average and a form-induced component,

$$\overline{\theta} = \langle\overline{\theta}\rangle + \widetilde{\overline{\theta}}, \tag{6}$$

where the overbar denotes time averaging, the angle brackets denote spatial averaging, and the tilde denotes the spatial deviation of the time-averaged quantity from its spatial mean. With these definitions, the double-averaged momentum and continuity equations may be written in the form given by Nikora et al. [15]:

$$\begin{aligned}\frac{\partial\langle\overline{u_i}\rangle}{\partial t} + \langle\overline{u_j}\rangle\frac{\partial\langle\overline{u_i}\rangle}{\partial x_j} = g_i - \frac{1}{\rho\phi}\frac{\partial(\phi\langle\overline{p}\rangle)}{\partial x_i} - \frac{1}{\phi}\frac{\partial\left(\phi\langle\widetilde{u}_i\widetilde{u}_j\rangle\right)}{\partial x_j} - \frac{1}{\phi}\frac{\partial\left(\phi\langle\overline{u_i'u_j'}\rangle\right)}{\partial x_j} \\ + \frac{1}{\phi}\frac{\partial}{\partial x_j}\left(\phi\left\langle\nu\overline{\frac{\partial u_i}{\partial x_j}}\right\rangle\right) + \frac{1}{\rho\phi}\frac{1}{V_f}\overline{\int_{S_{int}} p n_i\, dS} - \frac{1}{\phi}\frac{1}{V_f}\overline{\int_{S_{int}} \nu\frac{\partial u_i}{\partial x_j} n_j\, dS},\end{aligned} \tag{7}$$

and the continuity equation becomes

$$\left\langle\frac{\partial\rho}{\partial t} + \frac{\partial(\rho u_i)}{\partial x_i}\right\rangle = \rho\frac{\partial\phi}{\partial t} + \rho\frac{\partial(\phi\langle\overline{u_i}\rangle)}{\partial x_i} = 0. \tag{8}$$

In these expressions, u_i and u_j are the velocity components, g_i is the gravitational acceleration component, p is pressure, ρ is the fluid density, ν is the kinematic viscosity, and n_i is the component of the outward unit normal on the fluid–solid interface. The pressure and viscous surface-integral terms account for the momentum transfer between the flow and the surrounding bead structure. The term $\langle\widetilde{u}_i\widetilde{u}_j\rangle$ represents the form-induced, or dispersive, stress associated with spatial deviations of the time-averaged velocity, while $\langle\overline{u_i'u_j'}\rangle$ represents the Reynolds stress contribution associated with temporal fluctuations. This distinction is important for permeable-bed flows because the bed geometry produces spatial variations in the time-averaged motion that are not captured by Reynolds averaging alone.

In the present work, the double-averaging framework is used to interpret the measured velocity and stress fields above and within the porous bed. It provides a consistent way to separate mean flow, turbulent stresses, and form-induced stresses, which is why it is adopted here instead of relying only on a conventional Reynolds-averaged description.

The stress quantities reported in the following sections were computed from the measured velocity fields after time and spatial averaging. The viscous stress was evaluated from the vertical gradient of the double-averaged streamwise velocity, the turbulent stress from the Reynolds fluctuation product, and the dispersive stress from the spatial deviation of the time-averaged velocity field. The computed stress terms were then used to interpret the shear-stress balance and define the friction-velocity scale used for normalization. The

viscous and turbulent shear stresses are presented together in the shear stress section, while the dispersive contribution is presented separately because it arises from spatial heterogeneity of the time-averaged velocity field. This separation is particularly important for the present rough permeable bed because form-induced stresses cannot be assumed negligible a priori near the SWI.

3. Results and Discussion

In this section, experimental results for flow over and within rough permeable beds are presented. The RIM-PIV measurements described in Section 2 were used to obtain double-averaged profiles of mean velocity, viscous stresses, turbulent stresses, and dispersive stresses. The discussion begins with the mean velocity field and its vertical variation. Three experimental runs were performed for Re_K values of $Re_K = 0.224$, $Re_K = 0.335$, and $Re_K = 0.360$. Since all three cases remain below unity, they fall below the transition threshold typically associated with porous-bed turbulence [4,5]. Under these conditions, viscous effects are expected to remain important within much of the pore space, even though the overlying flow remains turbulent. The results are presented by first discussing the mean velocity and turbulence-intensity fields, followed by the viscous, turbulent, Reynolds, and dispersive stress distributions. In all vertical profiles, $z/d_p = 0$ denotes the SWI, $z/d_p < 0$ denotes the porous bed, and $z/d_p > 0$ denotes the overlying channel flow.

3.1. Mean Velocity Fields

Figure 4 shows the normalized mean streamwise velocity profiles. We normalize the velocity using the free-stream velocity above the bed, and the vertical coordinate is scaled by the bead diameter, z/d_p. This normalization enables comparison across flow rates while retaining the bead diameter as the geometric length scale. In all three cases, the velocity decreases rapidly within the porous region and becomes very small within roughly one bead diameter below the SWI. This trend is consistent with earlier experimental and numerical studies showing that the mean streamwise velocity decays exponentially within the porous bed, with the decay length scaling with permeability or particle size [3,16,17].

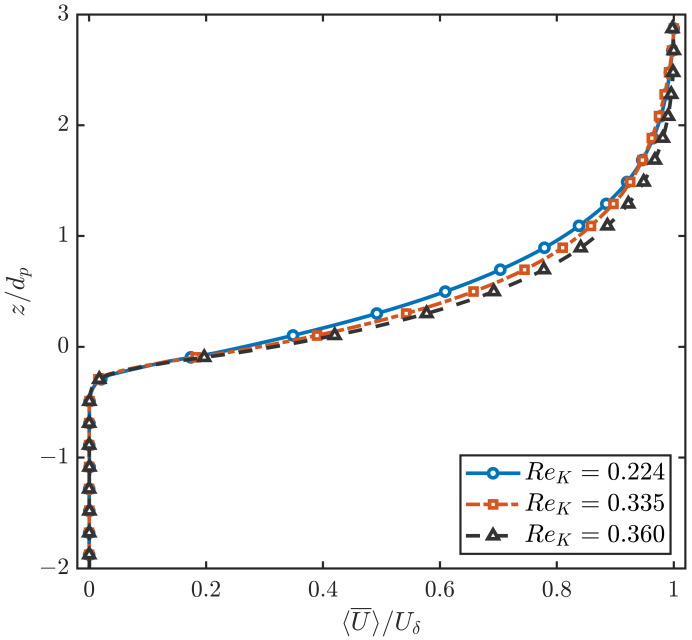

Figure 4. Dimensionless mean velocity profiles for the three RIM cases, corresponding to $Re_K = 0.224$, $Re_K = 0.335$, and $Re_K = 0.360$, respectively. The horizontal reference $z/d_p = 0$ denotes the SWI; negative values correspond to the porous bed and positive values correspond to the overlying flow.

Above the SWI, the velocity increases monotonically with height. The near-bed velocity gradient becomes steeper with increasing discharge, indicating stronger shear near the interface. In the outer region of the boundary layer ($z/d_p > 1.5$), the normalized velocity profiles collapse reasonably well, suggesting that the outer flow is less sensitive to changes in Re_K than the near-interface region.

Close to the SWI, the profiles separate more clearly. The $Re_K = 0.360$ case shows higher normalized velocities near the interface, whereas the $Re_K = 0.224$ case remains lower throughout this region. This indicates that outer-flow scaling captures the overall profile shape, but Reynolds number effects remain important close to the bed.

Although all cases remain in the low-Re_K regime, the velocity profiles show increasing shear and stronger near-interface motion as Re_K increases. Viscous effects still dominate within the porous layer and immediately above the SWI, but the outer flow becomes progressively more energetic with increasing discharge. Similar behavior has been reported in RIM studies by Rousseau et al. [16,25].

The profiles shown in Figure 4 demonstrate that the SWI serves as a narrow interface layer between the porous bed and the channel flow. The results show a steep velocity gradient in this region and indicate significant momentum exchange between the bed and the flow. This behavior shows that changes in Re_K influence the near-bed region and have a weaker effect on the outer profile. The flow above the bed responds mainly to channel-scale forcing, whereas the region close to and inside the bed remains strongly controlled by the local bed geometry and viscous resistance.

To further examine the near-bed response, Figure 5 presents six individual streamwise boundary-layer profiles extracted at distinct streamwise locations for $Re_K = 0.224$. The profiles retain the same overall boundary-layer form observed in the spatially averaged result, but they also reveal mild location-to-location variability in the thickness of the near-interface shear region. This indicates that even in the viscous-dominated regime, the local flow adjusts to small differences in bed configuration and local pore connectivity. At the same time, the six profiles remain reasonably clustered, which supports the conclusion that the mean flow structure in $Re_K = 0.224$, is repeatable, and is governed primarily by the combined influence of the overlying channel shear and the resistance imposed by the porous bed.

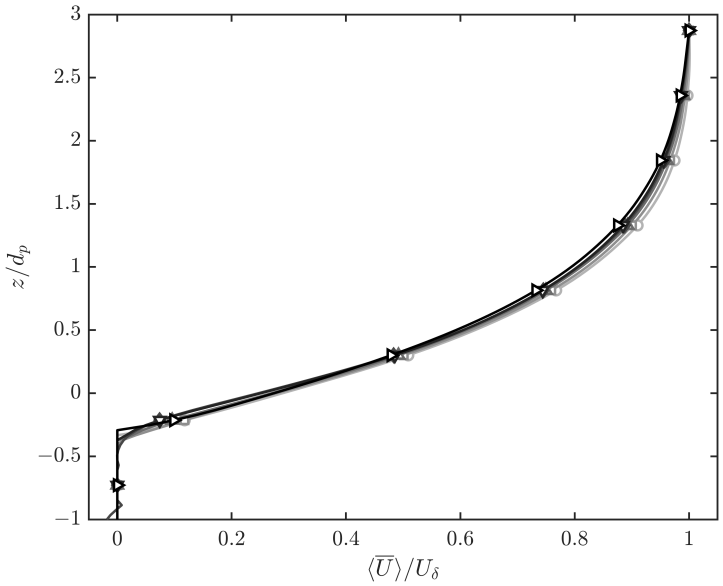

Figure 5. Six individual streamwise boundary-layer profiles extracted at distinct streamwise locations for $Re_K = 0.224$. The profiles show similar structure with modest spatial variability, indicating that the averaged velocity profile is not controlled by a single local bead arrangement.

The same qualitative behavior is observed for the other experimental runs. These profiles show that the main effect of increasing discharge is to strengthen the interfacial shear while preserving the same general vertical structure of the boundary layer. Thus, the streamwise comparisons complement the averaged profiles by showing that the measured trends are not confined to a single location but persist across the test section.

3.2. Turbulence Intensity Fields

Figures 6–8 show the turbulence-intensity fields for $Re_K = 0.224$, $Re_K = 0.335$, and $Re_K = 0.360$, respectively. These results extend the mean-velocity analysis by showing how the fluctuation levels vary with Re_K and distance from the SWI.

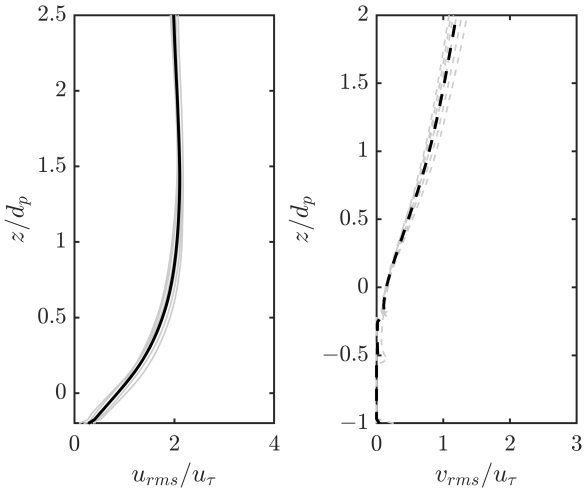

Figure 6. Turbulence-intensity field for $Re_K = 0.224$. The strongest fluctuations remain concentrated just above the SWI, while the porous region shows rapid damping of turbulent motion.

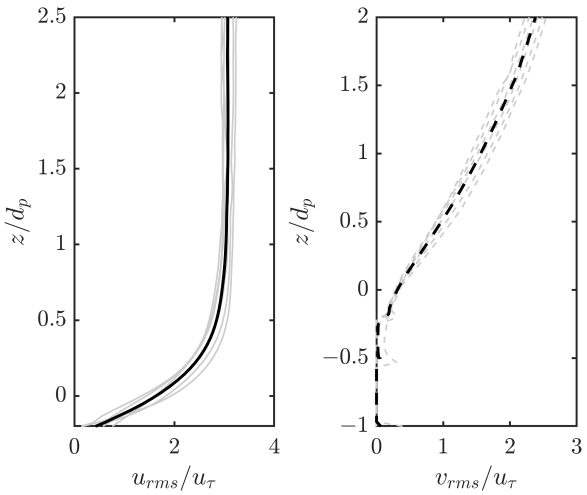

Figure 7. Turbulence -intensity field for $Re_K = 0.335$. Compared with $Re_K = 0.224$, the high-intensity region above the interface becomes more distinct and extends farther into the overlying flow.

Turbulence-intensity and turbulent-kinetic-energy measures are commonly used to identify regions of elevated fluctuations in hydraulic flows [26]. In all three cases, the largest turbulence intensities occur just above the interface, where the mean velocity gradient is also the largest. Below the SWI, the fluctuation levels decrease rapidly inside the porous bed, indicating strong damping of turbulent motion within the pore space. This behavior is consistent with the low-Re_K regime, where viscous effects remain important within the porous layer.

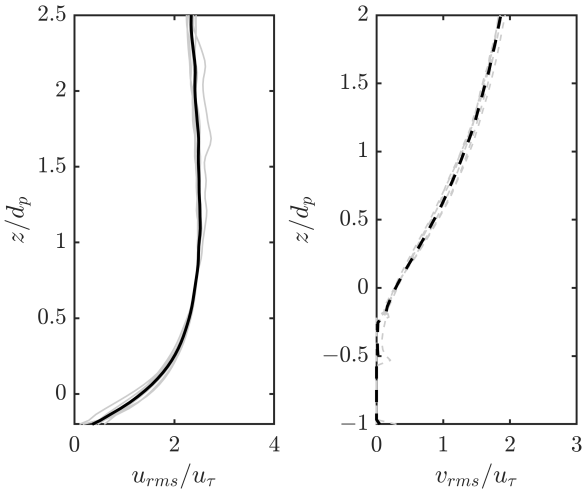

Figure 8. Turbulence -intensity field for $Re_K = 0.360$. The fluctuating region above the bed is strongest in this case, indicating the clearest growth in turbulent activity with increasing discharge.

The near-interface peak in turbulence intensity is also consistent with turbulence production associated with the interfacial shear layer. Similar peaks near the SWI have been reported in permeable-bed flows where the mean velocity changes rapidly across the interface [4,5,10]. However, the present measurements do not directly resolve coherent structures or instability modes, so the results only indicate a relationship with interfacial shear and do not identify a specific instability mechanism.

The data indicate that turbulence intensity grows gradually as Re_K increases. For $Re_K = 0.224$, the turbulence intensity remains relatively low and stays confined close to the interface. For $Re_K = 0.335$, the high-intensity region develops more clearly and extends farther into the flow above the bed. For $Re_K = 0.360$, the intensified region becomes strongest and spreads farther above the bed, showing stronger interaction with the interfacial shear layer.

These observations show that increasing Re_K affects the flow above the bed even within the low-Re_K regime. The bed-scale region remains strongly damped, while the overlying flow develops stronger fluctuations near the SWI as the Reynolds number increases.

The same comparison is consistent with the streamwise boundary-layer results discussed earlier. The six profiles for $Re_K = 0.224$ showed only modest location-to-location variability because the turbulence level near the interface was still limited. As the flow moves to $Re_K = 0.335$ and $Re_K = 0.360$, the stronger fluctuation field can increase the sensitivity of the near-interface region to local bed structure.

3.3. Shear Stress Distribution

Figure 9 shows the vertical distribution of total shear stress, normalized by ρu_τ^2, at three different permeability Reynolds numbers: $Re_K = 0.224$, $Re_K = 0.335$, and $Re_K = 0.360$. The three panels report the viscous stress (τ_v), the turbulent stress (τ_t), and the total stress ($\tau_{tot} = \tau_v + \tau_t$) as functions of the normalized vertical coordinate, z/d_p.

In a turbulent boundary layer, τ_v and τ_t carry momentum near the wall and decay toward the free stream. Within the porous region, the total stress is reduced and reflects weaker shear compared with the interface. Above the SWI, the total stress remains positive and decreases gradually away from the bed. The profiles indicate a gradual transfer of momentum away from the interface. The viscous stress decreases monotonically, while the turbulent stress rises first, reaches a peak in the transition region, and then decays. These results indicate that momentum transfer increases near the interface and decreases farther into the outer region.

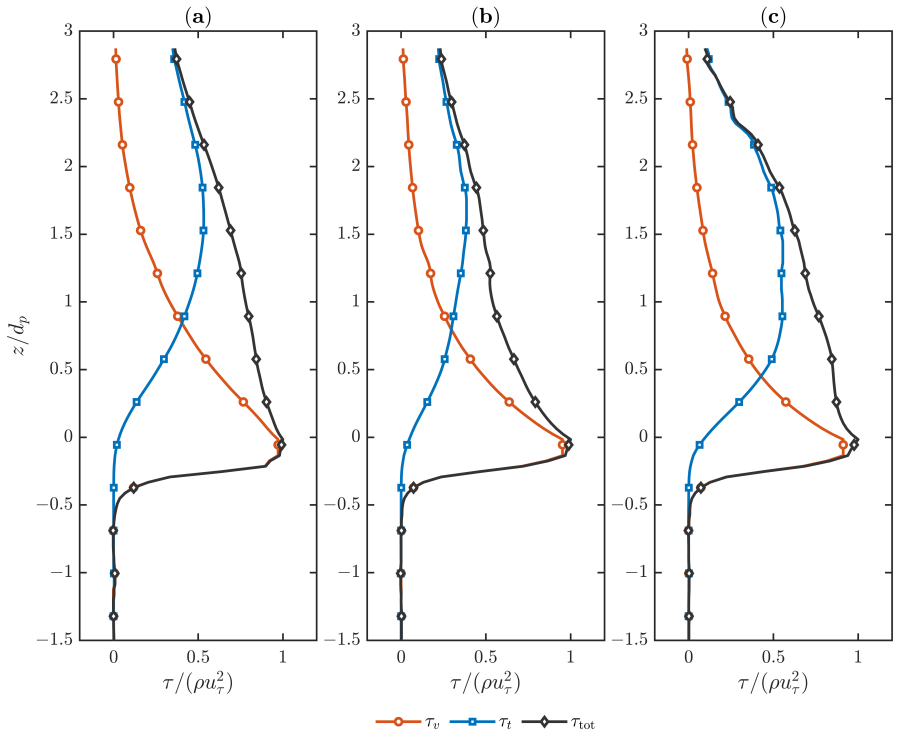

Figure 9. Normalized shear stress distributions for (**a**) $Re_K = 0.224$, (**b**) $Re_K = 0.335$, and (**c**) $Re_K = 0.360$. Each panel compares the viscous, turbulent, and total shear stress contributions as functions of the normalized vertical coordinate.

The balance between viscous and turbulent stress changes significantly with Re_K. At $Re_K = 0.224$, viscous shear dominates up to $z/d_p \approx 1$. The data show that turbulent stress overtakes viscous stress at about $z/d_p \approx 1$. As Re_K increases to $Re_K = 0.335$ and $Re_K = 0.360$, the crossing point shifts downward to approximately $z/d_p = 0.8$ and $z/d_p = 0.5$, respectively. These results suggest that the viscous sublayer becomes thinner and that Reynolds stresses play a larger role as the flow becomes more inertially dominated.

Inside the porous region, the stresses decrease rapidly to near-zero values and stay almost constant. This behavior indicates that pore-space resistance reduces momentum transport within the bed. It also indicates that turbulence penetrates only a short distance below the interface, so momentum transfer in the porous layer is limited and controlled mainly by viscous effects and form drag near the upper pore spaces.

3.4. Reynolds Stress Distribution

Figure 10 shows the normalized Reynolds stress distributions for the three flow cases: Reynolds 1, Reynolds 2, and Reynolds 3, corresponding to $Re_K = 0.224$, $Re_K = 0.335$, and $Re_K = 0.360$, respectively. The three profiles shown in each panel are the Reynolds shear stress, $-\overline{u'v'}^+$; the streamwise normal stress, $\overline{u'u'}^+$; and the wall-normal normal stress, $\overline{v'v'}^+$, plotted against the normalized vertical coordinate, z/d_p.

Inside the porous bed ($z/d_p < 0$), all three Reynolds stress components remain very small. This behavior is consistent with damping inside a rough permeable bed. The bed suppresses velocity fluctuations and limits turbulent momentum exchange below the interface. Similar damping of turbulence inside permeable beds has been reported in earlier work on permeable-wall and SWI flows [4,5].

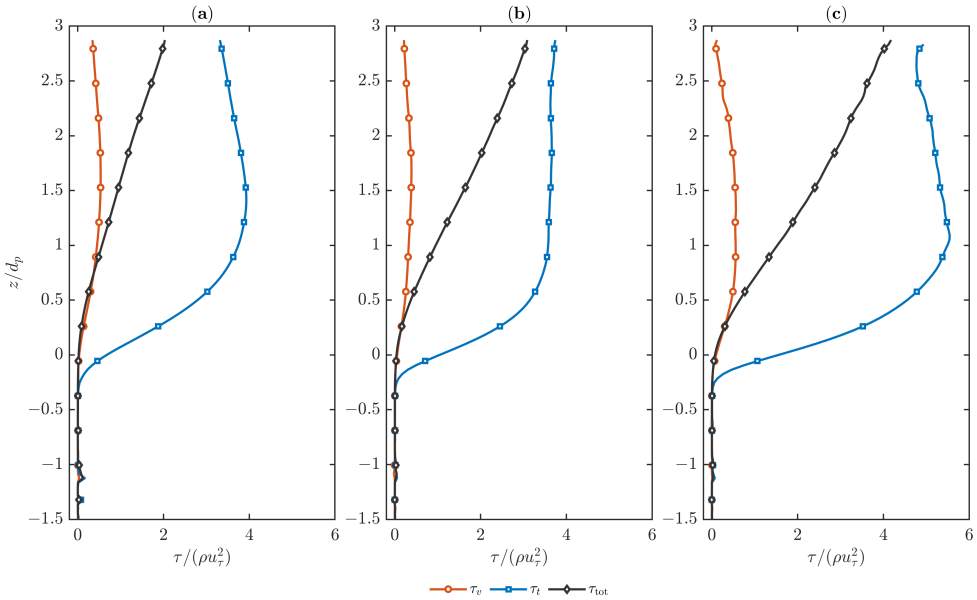

Figure 10. Normalized Reynolds stress distributions for (**a**) $Re_K = 0.224$, (**b**) $Re_K = 0.335$, and (**c**) $Re_K = 0.360$. The profiles show the Reynolds shear stress and the streamwise and wall-normal Reynolds normal stresses across the SWI.

Above the SWI, the Reynolds stresses increase quickly. The streamwise normal stress, $\overline{u'u'}^+$, is the largest component in all three cases and rises sharply just above the interface before approaching a broader outer-flow maximum. The wall-normal normal stress, $\overline{v'v'}^+$, also increases with height, but it remains smaller than $\overline{u'u'}^+$ over most of the profile. The Reynolds shear stress, $-\overline{u'v'}^+$, stays much smaller than the two normal-stress components and varies more gradually with height. This distribution is consistent with the idea that turbulence is generated near the interface and then redistributed into the overlying flow [4,5].

The overall shapes are similar in all three cases. The magnitude of the normal stresses above the interface increases with discharge. The $Re_K = 0.360$ case shows the clearest growth in both $\overline{u'u'}^+$ and $\overline{v'v'}^+$, but that change is gradual. The Reynolds shear stress also remains relatively small in all three cases, indicating that the normalized stress structure does not reorganize substantially over the present range of Re_K.

Overall, turbulent activity is weak inside the bed, concentrated near the interface, and stronger in the overlying flow. Increasing discharge, represented by increasing Re_K, strengthens that activity but does not produce a different Reynolds stress structure within the present experimental range.

3.5. Dispersive Stress Distribution

Figure 11 shows the double-averaged vertical profiles of dispersive stresses plotted between $z = -0.3d_p$ and $z = 0.9d_p$ for $Re_K = 0.224$, $Re_K = 0.335$, and $Re_K = 0.360$. Panels (a) and (b) show the square-root, RMS-like forms of the streamwise and wall-normal dispersive normal stresses, $\sqrt{\langle\tilde{u}^2\rangle_x}/u_*$ and $\sqrt{\langle\tilde{v}^2\rangle_x}/u_*$, normalized by u_*. Panel (c) shows the dispersive shear stress directly, $\langle\tilde{u}\tilde{v}\rangle_x/u_*^2$, normalized by u_*^2. The dispersive stresses reach their largest values near the interface and bead crests, as shown in Figure 11. Dispersive stresses arise from roughness-induced spatial heterogeneity in the time-averaged flow. The dispersive contribution is therefore most important close to the SWI and decreases away from the bed.

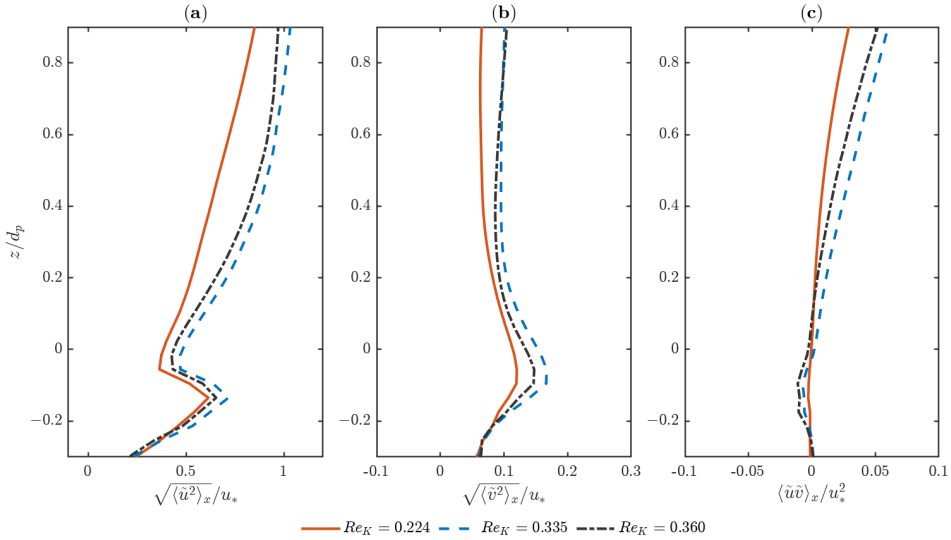

Figure 11. Normalized dispersive stress distributions for (**a**) square-root streamwise dispersive normal stress, $\sqrt{\langle\tilde{u}^2\rangle_x}/u_*$; (**b**) square-root wall-normal dispersive normal stress, $\sqrt{\langle\tilde{v}^2\rangle_x}/u_*$; and (**c**) dispersive shear stress, $\langle\tilde{u}\tilde{v}\rangle_x/u_*^2$, for $Re_K = 0.224$, $Re_K = 0.335$, and $Re_K = 0.360$, plotted against the normalized vertical coordinate, z/d_p. Panels (**a**,**b**) are presented in RMS-like form, while panel (**c**) is the directly normalized dispersive shear stress.

$\sqrt{\langle\tilde{u}^2\rangle_x}/u_*$increases above the bed and is larger than $\sqrt{\langle\tilde{v}^2\rangle_x}/u_*$ and $\langle\tilde{u}\tilde{v}\rangle_x/u_*^2$. This result indicates stronger spatial non-uniformity in the streamwise mean flow near the bed. The wall-normal dispersive normal stress, $\sqrt{\langle\tilde{v}^2\rangle_x}/u_*$, is smaller but follows a similar trend, with its largest value close to the interface. The dispersive shear stress, $\langle\tilde{u}\tilde{v}\rangle_x/u_*^2$, has the smallest magnitude and remains close to zero over most of the profile. Thus, the dispersive-stress contribution in these experiments is dominated by spatial non-uniformity of the mean streamwise motion rather than dispersive transfer of shear momentum.

Below the interface, the three curves come closer together and the dispersive stresses become smaller. This trend is consistent with damping of spatial variations in the mean flow within the porous bed. The dispersive stresses are therefore secondary to the stronger near-interface structure observed in the mean-velocity, turbulence-intensity, shear-stress, and Reynolds-stress results.

3.6. Conclusions

This study examined flow and stress distributions within a rough permeable bed for $Re_K = 0.224$, $Re_K = 0.335$, and $Re_K = 0.360$. The results show that the SWI is the main region controlling flow behavior. For all flow conditions studied, the SWI is a thin layer where momentum exchange and turbulence are largest. Below the SWI, velocity and turbulence decrease rapidly, indicating limited flow penetration into the bed. In addition, above the SWI, increasing Re_K increases velocity and turbulence while preserving the same overall flow structure. The analysis of turbulent, Reynolds, and total stresses shows that they remain close to the interface. Dispersive stresses are largest near the upper bead layer and bead crests, with the streamwise dispersive component dominant over the other components. The dispersive contribution remains smaller than the Reynolds-stress contribution. The findings also suggest that the porous bed does not act only as a rough boundary but also functions as a momentum filter that restricts the penetration of flow and turbulence into the bed.

Author Contributions: Conceptualization, Z.Q.M. and J.L.; methodology, Z.Q.M. and J.L.; formal analysis, Z.Q.M.; investigation, Z.Q.M.; writing—original draft preparation, Z.Q.M.; writing—review and editing, Z.Q.M.; supervision, J.L. Author J.L. passed away prior to the publication of this manuscript. All authors have read and agreed to the published version of the manuscript.

Funding: The authors acknowledge the U.S. Department of Energy's Office of Basic Energy Sciences (Geosciences), Grant DE-SC0021626. Z.M. acknowledges the support from the Fulbright Program.

Institutional Review Board Statement: Not applicable.

Informed Consent Statement: Not applicable.

Data Availability Statement: The data presented in this study are available from the corresponding author upon reasonable request.

Acknowledgments: The authors thank Sourabh Apte and Brian Wood for their assistance in developing the experimental flume and for their valuable discussions. The authors also thank Jordan Strahl for his contribution to the refractive-index-matching study.

Conflicts of Interest: The authors declare no conflicts of interest.

References

1. Brunke, M.; Gonser, T. The ecological significance of exchange processes between rivers and groundwater. *Freshw. Biol.* **1997**, *37*, 1–33. [CrossRef]
2. Findlay, S. Importance of surface-subsurface exchange in stream ecosystems: The hyporheic zone. *Limnol. Oceanogr.* **1995**, *40*, 159–164. [CrossRef]
3. Breugem, W.P.; Boersma, B.J. Direct numerical simulations of turbulent flow over a permeable wall using a direct and a continuum approach. *Phys. Fluids* **2006**, *18*, 025103. [CrossRef]
4. Manes, C.; Pokrajac, D.; McEwan, I.; Nikora, V. Turbulence structure of open channel flows over permeable and impermeable beds: A comparative study. *Phys. Fluids* **2009**, *21*, 125109. [CrossRef]
5. Voermans, J.; Ghisalberti, M.; Ivey, G. The variation of flow and turbulence across the sediment–water interface. *J. Fluid Mech.* **2017**, *824*, 413–437. [CrossRef]
6. Blois, G.; Best, J.L.; Sambrook Smith, G.H.; Hardy, R.J. Effect of bed permeability and hyporheic flow on turbulent flow over bed forms. *Geophys. Res. Lett.* **2014**, *41*, 6435–6442. [CrossRef]
7. Manes, C.; Poggi, D.; Ridolfi, L. Turbulent boundary layers over permeable walls: Scaling and near-wall structure. *J. Fluid Mech.* **2011**, *687*, 141–170. [CrossRef]
8. Chowdhury, M.N.; Khan, A.A.; Castro-Orgaz, O. A Numerical Approach to Analyzing Shallow Flows over Rough Surfaces. *Fluids* **2024**, *9*, 204. [CrossRef]
9. Zippe, H.J.; Graf, W.H. Turbulent boundary-layer flow over permeable and non-permeable rough surfaces. *J. Hydraul. Res.* **1983**, *21*, 51–65. [CrossRef]
10. Ghisalberti, M.; Nepf, H. Shallow flows over a permeable medium: The hydrodynamics of submerged aquatic canopies. *Transp. Porous Media* **2009**, *78*, 309–326. [CrossRef]
11. Voermans, J.J.; Ghisalberti, M.; Ivey, G.N. A model for mass transport across the sediment-water interface. *Water Resour. Res.* **2018**, *54*, 2799–2812. [CrossRef]
12. Strahl, J.D. Particle Image Velocimetry Study of Turbulent Flow over Porous Media Within and Above the Transitional Permeable Reynolds Number Regime. Ph.D. Thesis, Oregon State University, Corvallis, OR, USA, 2025.
13. Kuang, C.; Xing, W.; Zheng, Y.; Cong, X.; Wang, D.; Zou, Q. Effects of Artificial Reef Array Configuration on Turbulent Flow: PIV Experiment and Numerical Simulation. *Water* **2025**, *17*, 915. [CrossRef]
14. Biegowski, J.; Pietrzak, M.; Radosz, I.; Kaczmarek, L.M. Modelling of Granular Sediment Transport in Steady Flow over a Mobile Sloped Bed. *Water* **2024**, *16*, 2022. [CrossRef]
15. Nikora, V.; McEwan, I.; McLean, S.; Coleman, S.; Pokrajac, D.; Walters, R. Double-averaging concept for rough-bed open-channel and overland flows: Theoretical background. *J. Hydraul. Eng.* **2007**, *133*, 873–883. [CrossRef]
16. Rousseau, G.; Pascal, I.; Ancey, C. Modeling turbulent stream flows over rough permeable beds. In Proceedings of the 10th Conference on Fluvial Hydraulics, Delft, The Netherlands, 6–10 July 2020.
17. Karra, S.K.; Apte, S.V.; He, X.; Scheibe, T.D. Pore-resolved investigation of turbulent open channel flow over a randomly packed permeable sediment bed. *J. Fluid Mech.* **2023**, *971*, A23. [CrossRef]
18. Shen, G.; Yuan, J.; Phanikumar, M.S. Direct numerical simulations of turbulence and hyporheic mixing near sediment—Water interfaces. *J. Fluid Mech.* **2020**, *892*, A20. [CrossRef]

19. Karra, S.K.; Apte, S.V. Numerical investigation of turbulent flow over a randomly packed sediment bed using a variable porosity continuum model. *Phys. Fluids* **2024**, *36*, 115177. [CrossRef]
20. Memon, Z.; Strahl, J.; Liburdy, J.; Apte, S. Experimental Investigation of Flow over a Porous Bed Using PIV and PLIF. In *ASTFE Digital Library*; Begel House Inc.: Danbury, CT, USA, 2026.
21. Patil, V.A.; Liburdy, J.A. Scale estimation for turbulent flows in porous media. *Chem. Eng. Sci.* **2015**, *123*, 231–235. [CrossRef]
22. Roth, E.J.; Neupauer, R.M.; Mays, D.C.; Sather, L.J.; Crimaldi, J.P. Wall effect mitigation techniques for experiments with planar walls. *Transp. Porous Media* **2020**, *132*, 423–441. [CrossRef]
23. Mendes, L.P.; Ricardo, A.; Bernardino, A.J.; Ferreira, R.M. A hybrid PIV/Optical Flow method for incompressible turbulent flows. *Water* **2024**, *16*, 1021. [CrossRef]
24. Song, M.S.; Choi, H.Y.; Seong, J.H.; Kim, E.S. Matching-index-of-refraction of transparent 3D printing models for flow visualization. *Nucl. Eng. Des.* **2015**, *284*, 185–191. [CrossRef]
25. Rousseau, G.; Ancey, C. Scanning PIV of turbulent flows over and through rough porous beds using refractive index matching. *Exp. Fluids* **2020**, *61*, 172. [CrossRef]
26. Ikani, N.; Pu, J.H.; Soori, S. Flow pattern and turbulent kinetic energy analysis around tandem piers: Insights from k-ε modelling and acoustic doppler velocimetry measurements. *Water* **2025**, *17*, 1100. [CrossRef]